Noise Background Levels and Noise Event Tracking/Characterization Under the Arctic Ice Pack: Experiment, Data Analysis, and Modeling

Kevin L. Williams ⓘ , Michael L. Boyd, Alexander G. Soloway, Eric I. Thorsos, Steven G. Kargl, and Robert I. Odom

Abstract—In March 2014, an Arctic Line Arrays System (ALAS) was deployed as part of an experiment in the Beaufort Sea (approximate location 72.323 N, 146.490 W). The water depth was greater than 3500 m. The background noise levels in the frequency range from 1 Hz to 25 kHz were measured. The goal was to have a three-dimensional sparse array that would allow determination of the direction of sound sources out to hundreds of kilometers and both direction and range of sound sources out to 1–2 km from the center of the array. ALAS started recording data at 02:12 on March 10, 2014 (UTC). It recorded data nearly continuously at a sample rate of 50 kHz until 11:04 on March 24, 2014. Background noise spectral levels are presented for low and high floe-drift conditions. Tracking/characterization results for ice-cracking events (with signatures typically in the 10–2000-Hz band), including the initiation of an open lead within about 400 m of the array, and one seismic event (with a signature in the 1–40-Hz band) are presented. Results from simple modeling indicate that the signature of a lead formation may be a combination of both previously hypothesized physics and enhanced emissions near the ice plate critical frequency (where the flexural wave speed equals that of the water sound speed). For the seismic event, the T-wave arrival time results indicate that a significant amount of energy coupled to T-wave energy somewhere along the path between the earthquake and ALAS.

Index Terms—Arctic ambient noise, hyperbolic tracking.

I. Introduction

IN 2014, the Applied Physics Laboratory—University of Washington designed and constructed an Arctic Line Arrays System (ALAS) suitable for operations during the U.S. Navy Arctic Submarine Laboratory (ASL) Ice Experiment 2014 (ICEX14). ALAS comprises six vertical arrays spaced apart horizontally in a hexagonal pattern. It was constructed and deployed so as not to interfere with ongoing ASL exercises. Within this constraint, the goal was to have a 3-D sparse array that would allow determination of the direction of sound sources out to hundreds of kilometers and both direction and range of sound sources out to 1–2 km from the center of the array.

ALAS recorded both natural sounds (e.g., ice cracking, seismic-generated T-waves) and man-made sounds (e.g., planes and helicopters landing and taking off, snowmobile operations, etc.) that had frequency signatures in the 1-Hz–25-kHz band. ALAS started recording data at 02:12 on March 10, 2014 (UTC). It recorded data continuously (except for short periods where system checks were performed, hard drives and batteries swapped, or camp logistics prevented timely battery pack changes) at a sample rate of 50 kHz until 11:04 on March 24, 2014.

Ambient noise studies, including study of background noise levels, noise due to local ice cracking, and noise due to seismic events, have a long history [1]–[7]. Mechanisms associated with various ice-cracking noise signatures have been proposed. The initiation of a lead in close proximity (400 m) to ALAS presents a unique opportunity to examine proposed mechanisms relative to the noise signature measured from a single event. Results from simple modeling indicate that the signature of a lead formation may be a combination of both previously hypothesized physics and enhanced emissions near the ice plate critical frequency (where the flexural wave speed equals that of the water sound speed). The T-phase detection of a single, relatively local (400 km) seismic event also offers an opportunity to examine coupling of seismic energy into the water column. The experimental results are the main result of this paper and give an update to the noise environment in the current Arctic. Knowledge of the time dependent noise environment is essential when establishing performance limits on sonar systems. Establishing the levels, variations in those levels, and some of the physical mechanisms at play in the modern Arctic were the primary objectives of this paper. The modeling is used to qualitatively assess some of those physical mechanisms and also to indicate avenues where further effort could offer better physical insight.

The remainder of this paper is organized as follows. Section II describes the hardware used and the configuration realized during ICEX14. Section III details the method used to acoustically track the relative hydrophone locations of the array throughout the experiment. Section IV presents the results obtained for both the background ambient noise, and the detection and localization (in either angle or angle/range) of various events. Associated modeling is also included in that section. Section V discusses both the uniqueness of the data and possible future efforts.
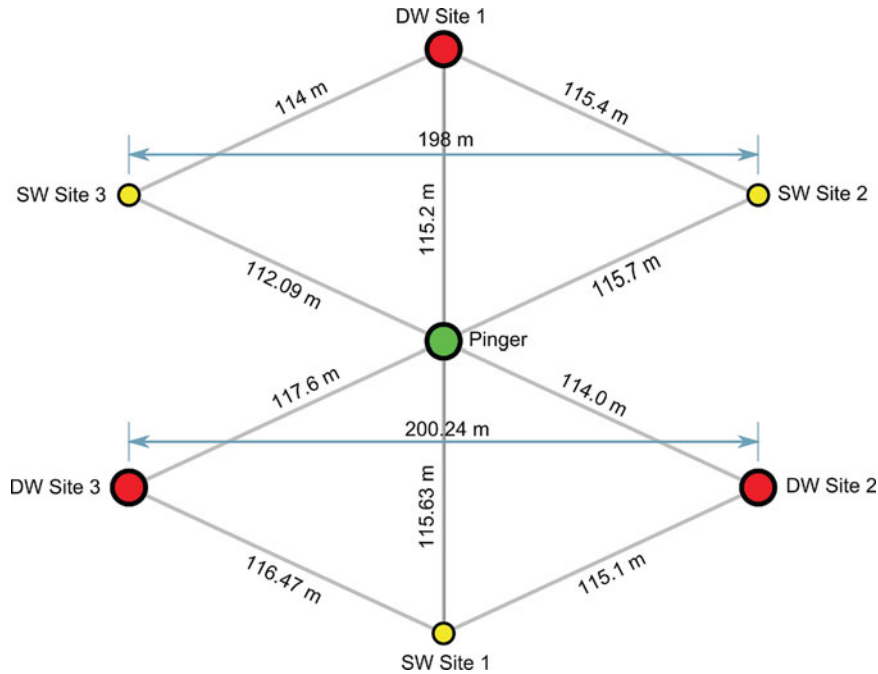
Fig. 1.　Horizontal geometry of ALAS hydrophone arrays as viewed from the top (as measured during deployment). The three red circles designate the top of the deep-water (DW) vertical arrays and the three yellow circles designate the top of the shallow-water (SW) vertical arrays.

II. EQUIPMENT

A. Hardware

ALAS is a battery-operated system to collect acoustic data from 6 two-element vertical acoustic arrays deployed under sea ice. The hydrophones used in the arrays were RESON TC-4032s (with a receive sensitivity of −164 dB re 1 V/μPa in the frequency range used). The Belden 8424 cables connecting the hydrophones to the surface were all wrapped with FAIR-WRAP cable fairing to reduce cable strum and thus allow viable data at the lowest frequencies of interest O(1 Hz). Each array also had at least one RBR Solo D Depth Recorder near the hydrophones to assist in determining the hydrophones relative positions. The arrays were strain relieved using Amsteel support line and weight was placed at the bottom of the arrays to combat cable streaming due to relative currents between the ice and the water.

Three of the arrays were deployed such that the deepest hydrophone was nominally at 30 m. The shallow hydrophone on these arrays was 3 m above the deep hydrophone. The other three arrays were deployed such that the deepest hydrophone was nominally at 80, 140, or 200 m. The shallow hydrophone on these arrays was 30 m above the deep hydrophone. The hydrophones were connected to a data acquisition (DAQ) system located in a small heated building on the ice. The entire system was run from lead–acid batteries and was electrically and physically isolated from the rest of the ICEX14 camp instrumentation. The DAQ building was located approximately 100 m from the main camp. Periodic maintenance was required to replace removable data hard drives, perform system checks, and carry out battery swapping as necessary. In addition to the arrays, an Applied Acoustics Underwater Technology LF Fatboy Beacon was deployed at 30-m depth that transmitted a 1-ms pulse centered at 15 kHz once an hour to aid in tracking the relative positions of the hydrophones in the arrays.

ALAS uses a Dewetron D313-16 Portable DAQ system with two ORION-0824-200 A/D Boards. The system features two removable 2.5-in hard drives. One drive is used for the operating system files, the other drive for data. Figs. 1 and 2 show a top view and a side view of ALAS, as deployed in ICEX14.

B. Deployment and Operations

The array deployment was accomplished through the use of a single centerline (made of nylon cord) and two laser range finders. The goal was to establish two nested equilateral triangles (one triangle formed by the yellow circles in Fig. 1, the other formed by the red circles in Fig. 1) in a hexagon shape each with 200-m sides. The ends of a deployed centerline defined positions for arrays labeled DW site 1 and SW site 1 in Fig. 1. The desired distance between these two points was 231 m (actual was 230.83 m). The center of the line was the location for the pinger. A partial hole in the ice was drilled at DW site 1, a surveying pole inserted and verified to be plumb with a carpenter level. A second survey pole was similarly set up at the location of the pinger and a third at SW site 1. The poles at DW site 1 and the pinger were used to survey in the locations of SW site 2 and SW site 3. This procedure was repeated using poles at SW site 1 and the pinger to survey in DW site 2 and DW site 3. At each of the surveyed locations a 6-in diameter hydrohole was drilled. The resulting, rangefinder-measured, horizontal locations, referenced to the pinger, are given in Fig. 1.

The (nominal) hydrophone vertical locations are shown in Fig. 2. The center of ALAS was approximately 700 m from
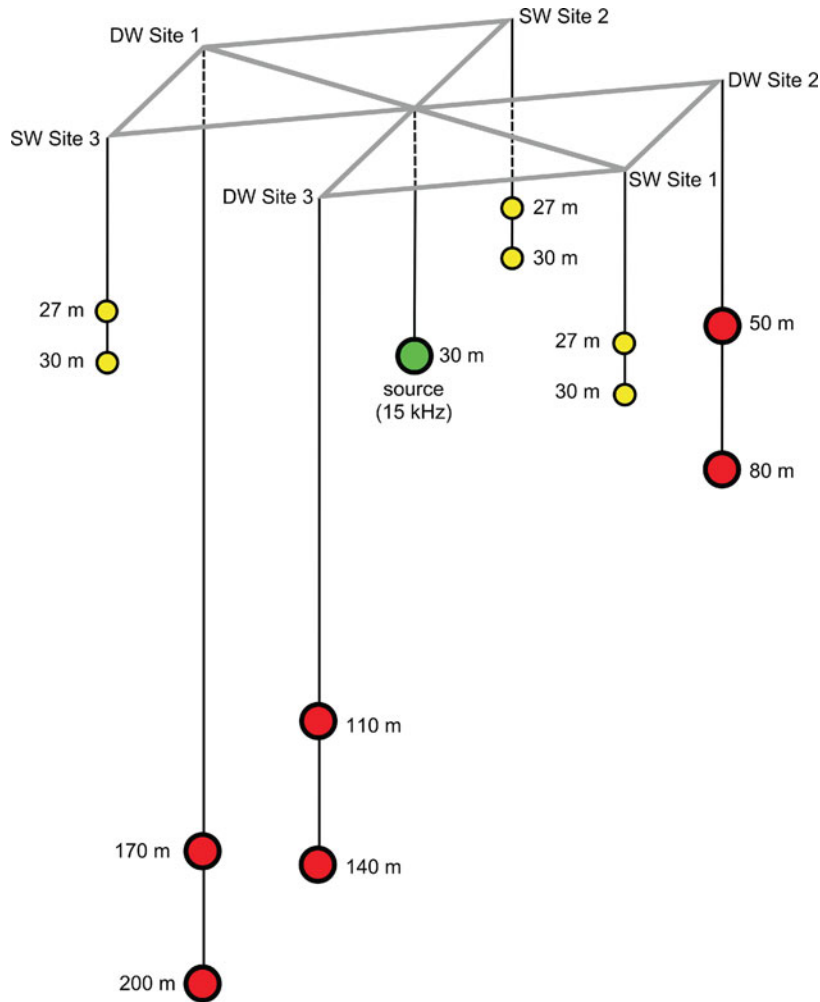
Fig. 2. Nominal vertical geometry of ALAS hydrophone arrays (note that actual positions are a function of ice drift conditions).

the center of the ice camp tracking system. The cabling from each of the hydrophones was deployed on the ice, back to the DAQ hut. Data with 60-s duration were stored in files for later analysis (1440 files for a full day of data). Each 60-s file was also analyzed using short-time Fourier transforms to look at the time frequency signatures of signals received.

III. ALAS HYDROPHONE TRACKING

Separate hydrophone localization schemes were chosen for the shallow and deep arrays. This was necessary as the shallow arrays had only a single depth sensor (on the upper hydrophone) while each hydrophone on the deep arrays had a devoted depth sensor. In both cases, straight-line ray acoustics was assumed since refraction effects were examined (using the measured sound-speed profile) and deemed small for our purposes. The salient point is that, once depth sensor data are used, the measured differences in the time delays between the 15-kHz source and all hydrophones can be used to solve for one variable, the azimuthal angle ϕ about the vertical z-axis. This is a variation of the well-known technique known as hyperbolic tracking [8].

The model chosen for the deep arrays has the associated geometry, as shown in Fig. 3. This model utilizes a polar coordinate system where the positions of the hydrophones relative to the mounting location (X_o, Y_o, Z_o) is determined by a radial position (r_U for the upper hydrophone and $r_U + r_L$ for the lower hydrophone) and the azimuthal angle ϕ about the z-axis (where ϕ is measured relative to the x-axis). The shallow array geometry is similar but assumes the array cable is straight.

Finding r_U and r_L involved the following steps. The depth of the upper hydrophone Z_U was found from the corresponding depth sensor (depth sensor accuracy is better than 1 cm). The lower hydrophone position Z_L was found by subtracting Z_U from the lower depth sensor measurement (i.e., $Z_L =$ (depth)$_L$-Z_U). In-field alterations during deployment make the depth sensors the most reliable estimate of line lengths L_L and L_U. (Securing strain relief cables after deployment resulted in changes to depths realized for the hydrophones.)

To find the line lengths L_L and L_U, the maximum depth recorded by the depth sensors over the time period of interest was used (there were several periods in which the relative ice/water motion was at or near zero and the hydrophone cables were vertical). Having determined Z_U, Z_L, L_L, and L_U, one can find
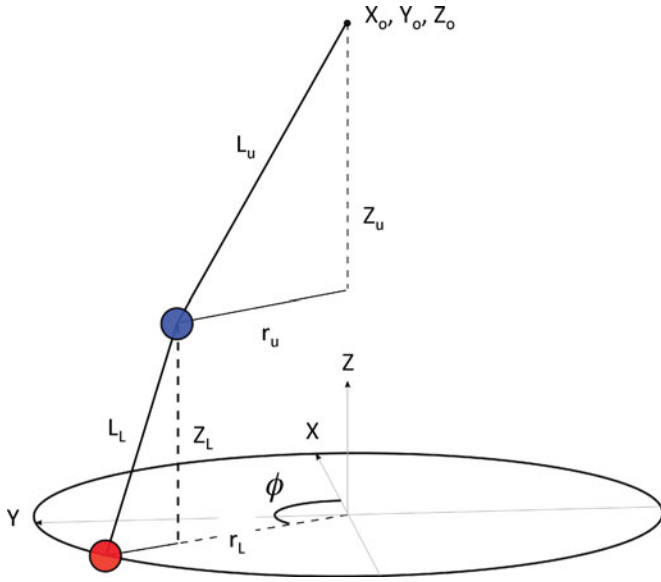
Fig. 3.   Simple model used in tracking the three deepest hydrophone arrays. Note that r_L denotes the solid portion of the line.
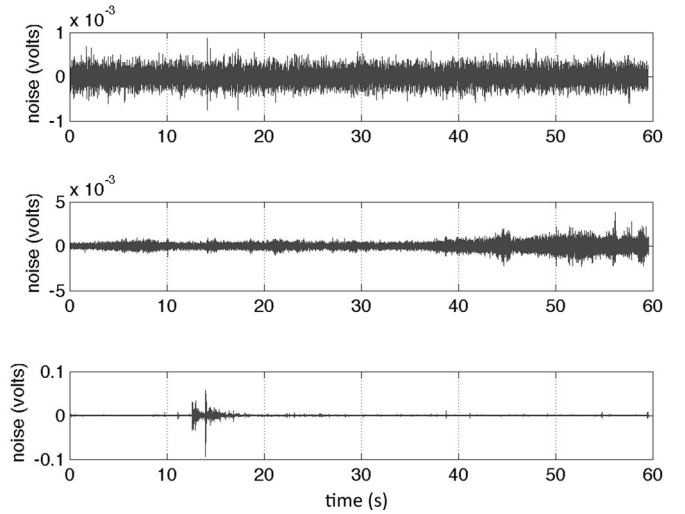

Fig. 4.   Top plot is for a particularly quiet time, the middle shows the signal as a helicopter spins up its rotors, and the bottom is an ice-cracking event. (Note the differing vertical scales.) The identifications come from listening to audio versions of these files.

r_U and r_L from simple geometry as follows:

$$r_U = (L_U{}^2 - Z_U{}^2)^{1/2} \qquad (1)$$

$$r_L = (L_L{}^2 - Z_L{}^2)^{1/2}. \qquad (2)$$

The *X* and *Y* positions of the hydrophones are then given by

$$X_U = X_o + r_U \cos(\phi) \qquad (3)$$

$$Y_U = Y_o + r_U \sin(\phi) \qquad (4)$$

$$X_L = X_o + (r_U + r_L)\cos(\phi) \qquad (5)$$

$$Y_L = Y_o + (r_U + r_L)\sin(\phi). \qquad (6)$$

Calculation of the arrival time delay between the 15-kHz source and each receiver was carried out using a cross correlation. To determine the position of the hydrophones the source position was assumed (see discussion below) and the receive time at hydrophone i was computed for the hydrophone positions $(X_{i,\phi}, Y_{i,\phi}, Z_{i,\phi})$ for all azimuthal angles in $1°$ increments

$$\Delta t_i{}^\phi = ((X_{i,\phi}{}^2 - X_s{}^2) \qquad (7)$$

$$+ (Y_{i,\phi}{}^2 - Y_s{}^2) \qquad (8)$$

$$+ (Z_{i,\phi}{}^2 - Z_s{}^2))^{1/2}/c_w \qquad (9)$$

where c_w is the sound speed in the water (chosen to be 1440 m/s based on measured sound-speed profiles) and (X_s, Y_s, Z_s) is the source location. Having obtained the source–receiver travel time, the difference in arrival time between hydrophone i and j for each angle ϕ is computed, denoted as $\delta^\phi_{i,j}$

$$\delta^\phi_{i,j} = \Delta t_i{}^\phi - \Delta t_j{}^\phi. \qquad (10)$$

The best fit is given by the ϕ that minimizes the sum of the mean square error between the modeled arrival time differences $\delta^\phi_{i,j}$ and the actual arrival time differences $\delta_{i,j}$ for the 12 hydrophones. (Note that arrival time differences are needed since the transmitter is not synched to the receivers.)

The source line length was approximately 30 m. Since no depth sensor was placed on the source, its depth Z_s was assumed to be equal to the average of the lower hydrophone depths on the shallow arrays and the source line was assumed to be vertical (i.e., $X_s = Y_s = 0$). The angle ϕ determined by the error minimization is relatively insensitive to variations in the assumed source position on the order of meters. The tracking results allow the relative positions of all hydrophones to be estimated [errors of O(10 cm) were found in tests using simulated data] at any point in time during the experiment (with 1-h resolution).

Once the hydrophones were tracked using the known source location, the same procedure was used to track the unknown locations of sources such as ice-cracking and seismic events. For sources within about 2 km from the array, Monte Carlo simulations over 10 000 random source locations indicated that positions of unknown sources could be located to a standard deviation of less than 5 m. For longer range sources, the standard deviation increased quickly with range but the uncertainty of the angle of arrival remained small (2–3°) regardless of range. This is a well-known behavior of hyperbolic tracking [8].

IV. BACKGROUND AMBIENT NOISE AND NOISE EVENTS

A. Examples of Analysis Results

Fig. 4 shows three 60-s time signals from the deepest hydrophone (DW site 1, 200-m depth). The top plot is for a particularly quiet time, the middle shows the signal as a helicopter is spinning up its rotors, and the bottom is an ice-cracking event. The identifications come from listening to audio versions of these files.

When the hydrophone calibration is taken into account, the spectral densities in Fig. 5 are obtained from the time signals of Fig. 4. The narrow peaks seen in the black curve of Fig. 5 are associated with ice camp equipment. Comparison of the results in Fig. 5 (and those to be shown in later plots) with previous
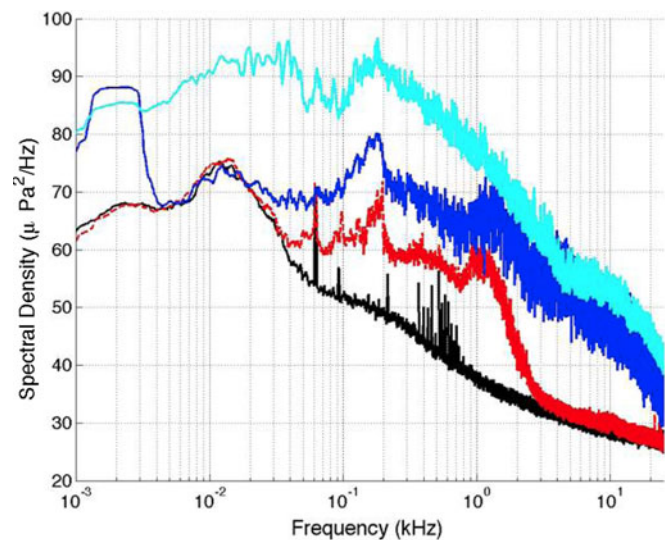
Fig. 5. Ambient noise spectral densities (vertical scale is in dB re 1 μPa^2/Hz). Black curve corresponds to top plot in Fig. 4, red to the middle plot, and blue to the bottom plot. The cyan curve is from a local ice-cracking event on March 16, approximately 400-m range from the ALAS array.

Fig. 7. Time/frequency signature of the ice-cracking event on March 16 referred to in Fig. 5. This is the same data as in the top panel of Fig. 6 but with a logarithmic frequency scale. Color bars are in dB re 1 μPa^2/Hz.
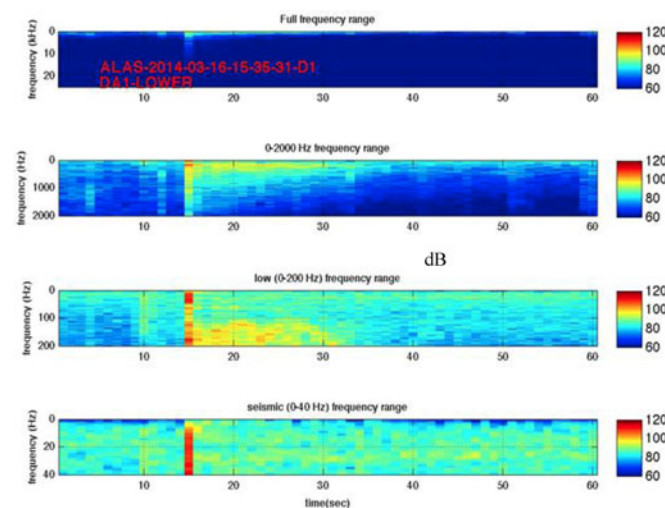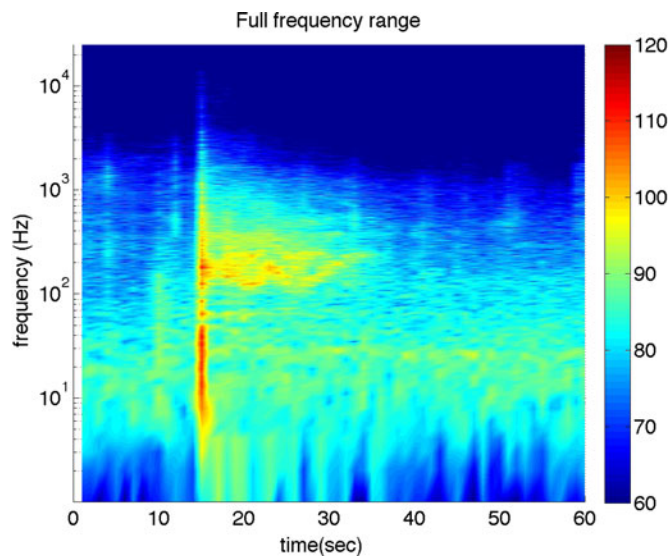

Fig. 6. Time/frequency signature of the ice-cracking event on March 16 referred to in Fig. 5. Note that the four panels span different frequency ranges so that the details in different frequency bands can be examined. Color bars are in dB re 1 μPa^2/Hz.
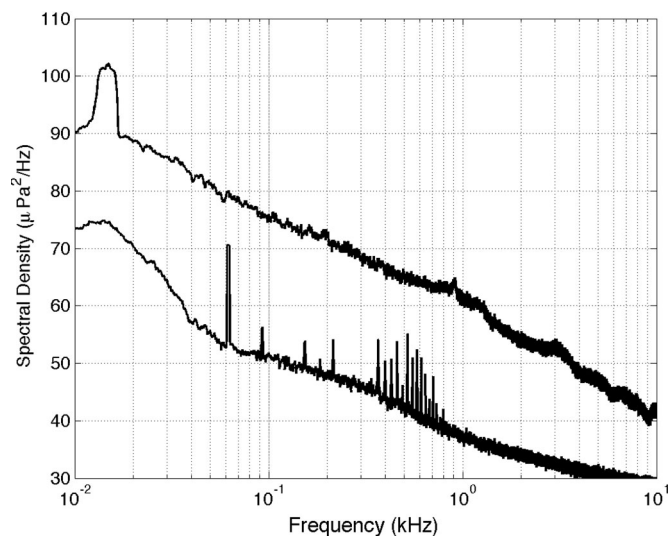

Fig. 8. Background noise spectral density for low (lower curve) and high (upper curve) wind speeds. (Vertical scale is in dB re 1 μPa^2/Hz.)

results [3, Fig. 5] indicates that in the 1–100-Hz band the lowest ambient noise level during ICEX14 (at least during initial camp buildup) was approximately 10 dB lower than that in the mid-Arctic ridge region of [3]. The peak noise level here and in [3] occurs near 10 Hz. A possible explanation for this peak, a combined effect of the spectrum of ice ridging events with propagation filtering, has been given previously [9]. A possible reason for the similar structure in the red and blue curves is mentioned at the end of Section IV-D. (Note also that the peak in the blue curve below 10 Hz is associated with cable strum.)

As discussed earlier, each 60-s file was also analyzed using short-time Fourier transforms to look at the time frequency signatures of signals received. An example of this analysis is shown in Fig. 6. Four panels are shown so that the detailed structure over different frequency bands can be examined. Fig. 7 is the

same data as the top panel in Fig. 6 but with a logarithmic frequency scale allowing a different view of the data. The example shown corresponds to the ice-cracking event on March 16 whose spectrum is shown in Fig. 5. As was evident in Fig. 5, this type of impulsive ice-cracking event creates acoustic energy over the entire 1-Hz–25-kHz band. Note also, the very long tail (over 10 s) of energy in the 100-Hz–1-kHz band. This will be a subject of discussion later in this paper. Figs. 4–7 represent prototypical examples of the results to be discussed below.

B. Background Noise Levels

Fig. 8 shows measured background noise levels during what were identified as low and high wind speed conditions and when there were no local ice-cracking events. Since meteorological
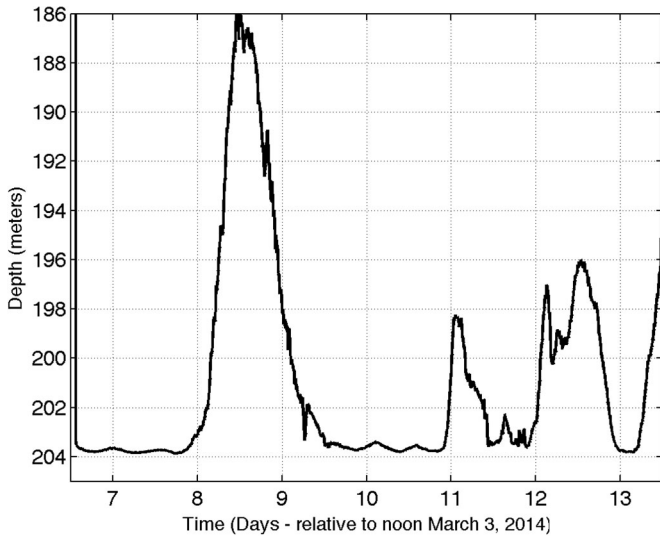
Fig. 9.   Depth measured on longest line of Fig. 2 as a function of time. The noise levels shown in Fig. 8 were taken at days 7.0 and 8.5 of this figure. At 7.0 the wind speed was near zero and at 8.5 the wind speed was greater than 20 m/s. Note that the data at the beginning and end of the time window indicate readings as the equipment was deployed (beginning) and then raised to 30-m depth (end).
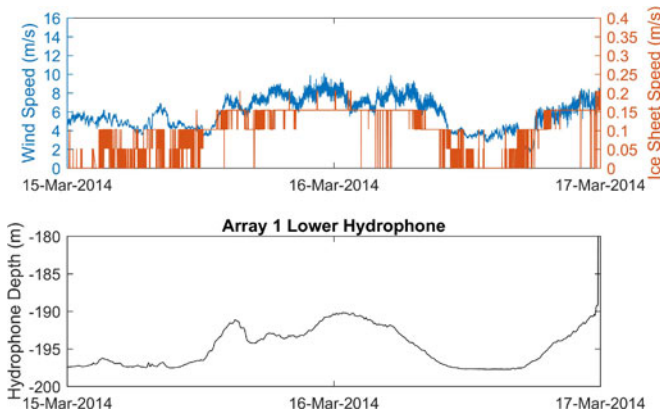

Fig. 10.   Meteorological data are shown in the top panel and depth recorded for the deepest pressure sensor in the bottom panel.

Fig. 11.   Ambient noise for four days: from top to bottom—March 10, 12, 14, and 16, respectively. Color bars are in dB re 1 μPa^2/Hz. The high noise levels seen in the bottom panels around 10 kHz are from a camp pinger. The two curves in Fig. 8 bound the overall variations seen in this figure. Exceptions to this are when there are narrow vertical lines, often indicative of ice cracking.
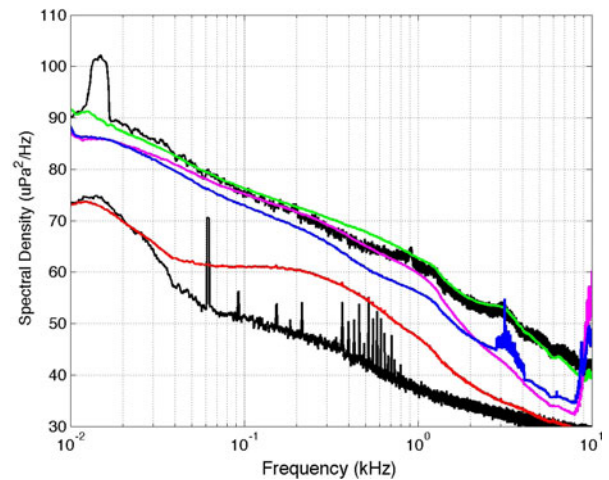
Fig. 12.   Average spectral levels for each day in Fig. 11 (red—March 10, green—March 12, magenta—March 14, and blue—March 16) as well as the two curves in Fig. 8 are shown. The curves in Fig. 8 essentially bound the daily averages.

data were not available before March 15, the depth measured for the deepest hydrophone was used as a proxy for wind speed. Fig. 9 shows the depth recorded for the deepest pressure sensor as a function of time relative to UTC noon on March 3. Using changes in depth as a proxy of wind speed (as the hydrophone "kites" due to relative ice/water movement) was shown viable by comparing meteorological data from later in the experiment to depth measurements during that later time. (Fig. 10 shows meteorological data in top panel and depth recorded for one of the pressure sensors in the bottom panel. Comparison in the March 15–17 timeframe indicates the viability of the proxy.) The noise levels shown in Fig. 8 were taken at days 7.0 and 8.5 on Fig 9. At 7.0 the wind speed was near zero and at 8.5 the wind speed was greater than 20 m/s.

Note that the high wind speed curve in Fig. 8 has an artificially high peak at around 16 Hz due to the effects of cable strum; however, it still seems appropriate to infer a peak in the true
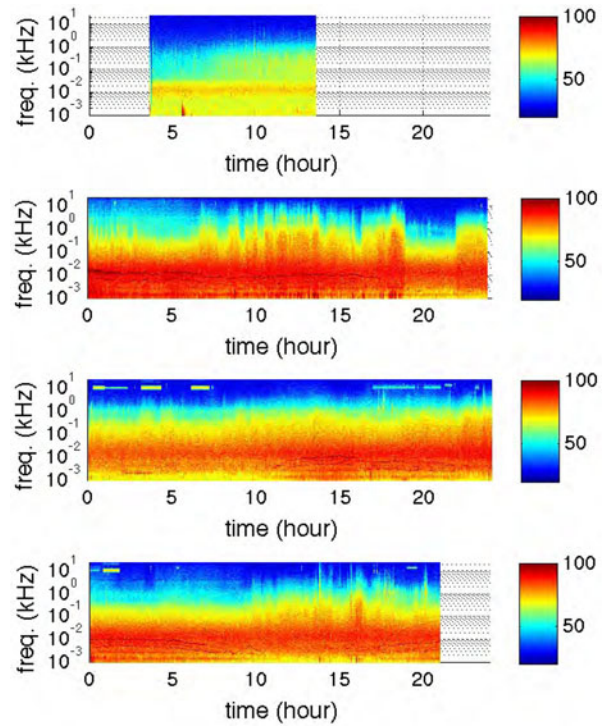
spectral level at around 10–20 Hz, seen also in the lower wind speed curve. This is a well-known peak for Arctic ambient noise [7]. Also, the low wind speed curve in Fig. 8 shows several isolated spectral lines associated with ice camp equipment.

Before proceeding to noise events, it is useful to give an indication of ambient noise variations over long time scales (hours). The temporal resolution does not allow a clear view of short time scale events such as cracking but does allow one to see variations in ambient noise as long time scale conditions

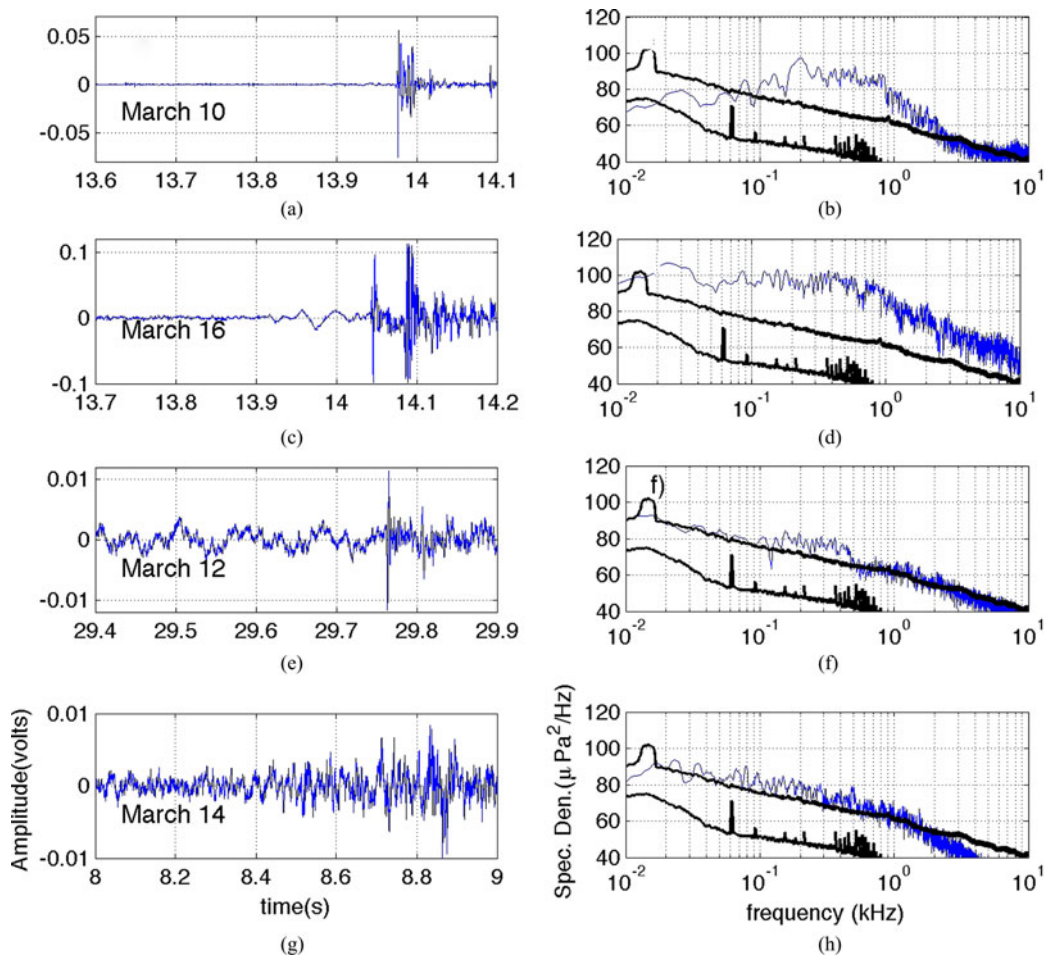Fig. 13. Time signatures for four representative ice-cracking events are shown on the left side. The time axis indicates seconds relative to the associated time of data given in Table I. The right side shows the corresponding spectral densities determined from the time signals and the receiver sensitivity. Fig. 13(a)–(d) is associated with times of low wind speed and Fig. 13(e)–(h) is associated with times of high wind speed. Also shown in the panels on the right are the high and low wind speed background noise curves from Fig. 8.

change. Fig. 11 shows ambient noise in a similar manner to Fig. 7 but over the entire days of March 10, 12, 14, and 16. These dates are chosen because the next section looks at noise-cracking events within those days. Note the horizontal time window where data are available is different on different days due to periodic equipment failure and time needed for recovery.

The background noise levels in Fig. 11 can be compared to Fig. 9, again using that figure as a proxy for wind speed and remembering that the labeled days on the *x*-axis in Fig. 9 are relative to noon on March 3. The spectral lines often seen below 10 Hz in Fig. 11 are strum resonances and are indicative of high wind speed conditions. Their existence is well correlated to the high wind speed conditions in Fig. 9. The high noise levels seen in the bottom panels of Fig. 11 around 10 kHz are from a camp pinger. Fig. 12 shows averages of each day in Fig. 11 as well as the two curves in Fig. 8, the curves in Fig. 8 essentially bound the daily averages. Narrow vertical lines in Fig. 11 are often indicative of ice cracking. Looking at those lines with more temporal detail give results such as that shown in Fig. 7. In the following section, several of these ice-cracking events are examined in more detail.

C. Noise Events—Ice Cracking

Ice-cracking events were initially identified from time-domain signals, the spectrograms, and from listening to audio signals. In practice, an initial thresholding algorithm looked for large events relative to the background (determined from several 60-s files near the file being examined) in the time domain, spectrograms of these events were made and audio files were generated from which cracking events could be separated from anthropogenic ones. Over 100 ice-cracking events were detected by this rudimentary methodology. The time signatures for four representative ice-cracking events are shown on the left side of Fig. 13 using the data from the hydrophone at 140-m depth (spectral densities at other depths overlapped the ones shown). The right side shows the corresponding spectral densities determined from the time signals (using the time window shown in the appropriate left side panel) and the receiver sensitivity. Also shown in the panels on the right are the two curves from Fig. 8 to allow an indication of detectability under different wind conditions. The event that occurred closest to ALAS is shown in Fig. 13(a) and the one furthest from ALAS in Fig. 13(g). The time of day (i.e., the beginning of the one minute file in which

TABLE I
DATE, TIME OF DAY (I.E., THE BEGINNING OF THE ONE MINUTE FILE IN WHICH THE DATA ARE LOCATED), AND TRACKED LOCATION (RELATIVE TO ALAS ORIGIN) OF THE FOUR EVENTS SHOWN IN FIG. 13

Date	Time of day (UTC)	x location (m)	y location (m)
March 16 (low-frequency precursor)	15:35:31	65	55
March 16 (first high-frequency pulse)	15:35:31	425	455
March 16 (second high-frequency pulse)	15:35:31	325	355
March 10	13:18:52	270	260
March 12	06:17:07	−630	320
March 14	04:53:48	1580	−980

For March 16, the locations are given for the low-frequency precursor signal and the two higher frequency pulses seen in Fig. 13(c). The locations for all but the longest range are given to +/− 5 m in keeping with standard deviations seen in simulations. The longest range is given to +/− 10 m for the same reason.

the data are located) and locations relative to ALAS, as determined from tracking using the hydrophone positions at the time of each event, are shown in Table I. The prototypical examples shown span the types of time and spectral level signatures seen. The March 16 event being the loudest and the March 14 being right at the limit of detectability using our somewhat crude detection method.

Fig. 13(a)–(d) is associated with times of low wind speed and Fig. 13(e)–(h) is associated with times of high wind speed. The event in Fig. 13(a) and (b) has much lower spectral density at the lowest frequencies, indeed the level at 10 Hz is at the low wind speed background level. The spectrum for this event is similar to that shown previously as associated with the direct signal from an ice-cracking event [2], [6]. In [6], the spectrum is associated with the propagation speed and coherent length (individual cracking initiation points and length of the crack associated with each point) of the ice-cracking event. In that reference, a low frequency (200 Hz) precursor was also detected as well as a high frequency (5000 Hz) signal. Equivalent signals are not seen in the data presented here. (Though precursors exist in some of the data examined here they are centered at much lower frequencies and thus we do not believe they are due to the physics described in [6].)

Fig. 13(f) and (h) shows low-frequency signatures that cannot be definitively associated with the event itself because these data were taken during high wind speed conditions and the events were further away (cf., Table I). Separate from this low frequency (<100 Hz) region there is at least an indication that the spectra of these two events are similar to the one in the top panel.

D. Noise Events—Ice Cracking Associated With Lead Formation

The event on March 16 [see Fig. 13(c) and (d)] is unique among the events shown in that it is definitively associated with the initial formation of an open lead that continued to expand during the course of the day. It was among the loudest events seen during the period of ALAS deployment and has
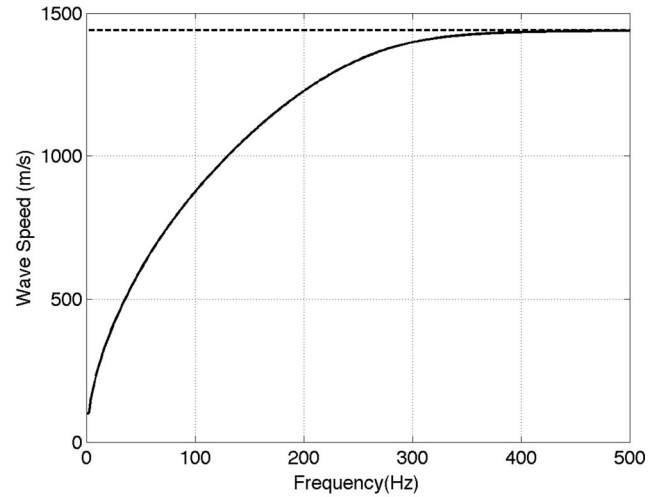

Fig. 14. Dispersion curve (solid line) of the a_{o-} wave for a 2-m-thick ice sheet with the parameters given in the text. The dashed line is the speed of sound in water.

signature across the entire frequency band. This type of event has been proposed as one source of the low-frequency peak at around 10–20 Hz in Arctic noise spectra [7]. (It is this event that is shown in Figs. 6 and 7. In those figures, it is evident that the event signature continues for at least 10 s after the initial arrival.) The event is further dissected below. Before doing so however, some background on the acoustics of plates loaded on one side by a fluid is useful. At low frequencies, plates support the propagation of both symmetric and antisymmetric "Lamb" waves. It is important to note that true antisymmetric Lamb waves are associated with plates in vacuum; for a fluid-loaded plate, the appropriate mode is known as the a_{o-} wave [10]. Below the critical frequency, the antisymmetric Lamb wave has a wave speed less than that of the fluid. For frequencies above but near the critical frequency (where the antisymmetric Lamb wave dispersion curve for a plate in vacuum equals that of the fluid), the plate is known to radiate with high efficiency [11]. This critical frequency is given by

$$f_c = \frac{1}{2\pi} c_f{}^2 \sqrt{\frac{12\rho(1-\sigma^2)}{h^2 Y}} \tag{11}$$

where Y and σ are the Young modulus and Poisson ratio of the plate, respectively, h is the plate thickness, ρ is the plate density, and c_f is the speed of sound in the fluid. Above the critical frequency, the associated radiation efficiency is proportional to $1/\sqrt{k^2 - k_f{}^2}$ (cf., [12, Appendix A] for the case of Rayleigh waves), where k is the flexural wave wavenumber and k_f is the wavenumber in the water. For shells, enhancements in backscattering near this frequency have been demonstrated [10]. Using typical sea ice longitudinal and shear speeds of $c_l = 3564$ m/s and $c_s = 1705$ m/s [13] and an approximate ice density of 900 kg/m^3, a Young modulus of 7.0×10^9 N/m^2 and a Poisson ratio of 0.34 can be calculated. For 2-m-thick ice (the approximate thickness in the region of ALAS during the time of its operation) and a water sound speed of 1440 m/s, (11) gives an f_c of about 190 Hz.
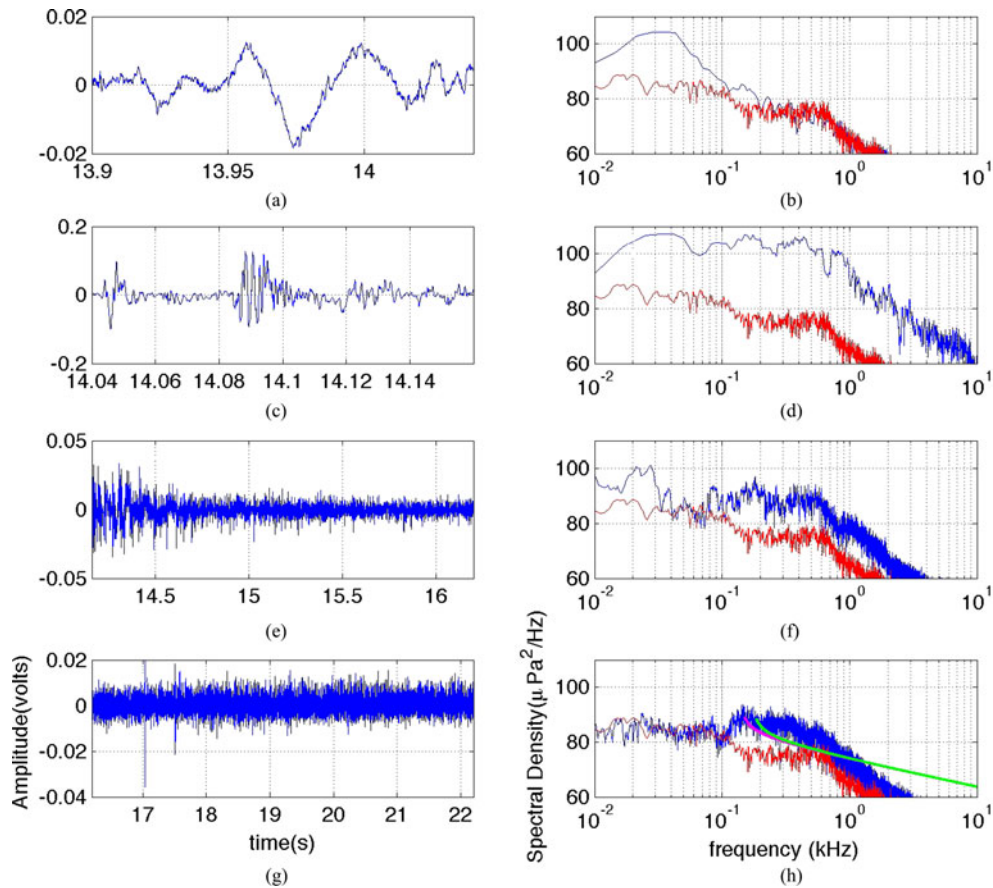
Fig. 15. Cracking event associated with the March 16 lead formation is shown, the time period from 13.9 to 22.1 s is split so as to look at the evolution of the spectral content. Fig. 15(a) shows the low-frequency precursor seen in Fig. 13(c) starting at about 13.9 s. Fig. 15(b) shows both the spectrum of this precursor time window (blue) and the background spectrum from several seconds before the event (red). This same background is shown on all the panels on the right. The remaining panels indicate the transition from a signal with main contributions in the tens of hertz to one with contributions from 10 Hz to 10 kHz and finally to one whose main contribution is in the hundreds of hertz. Fig. 15(h) also shows magenta and green curves that indicate the relative radiation efficiency of the supersonic flexural wave. See text for more details.
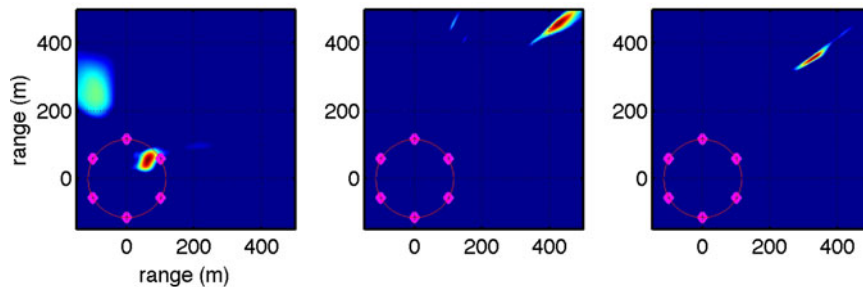

Fig. 16. March 16 tracking results. The magenta diamonds show the horizontal locations for the ALAS array. The red areas are the tracked locations of the events seen in Fig. 15(a) and (c). These correspond to the March 16 locations given in Table I. The left side of the figure shows the tracking result for the low-frequency precursor in Fig. 15(a). The middle and right panels are the tracking results for the first and second pulses seen in Fig 15(c). See text for more details.

The reality of the a_{o-} mode behavior is more complicated than described using the antisymmetric Lamb wave dispersion curve for a plate in a vacuum. In particular, the a_{o-} mode is dispersive but the wave speed never exceeds that of water (because of this and its limiting behavior at high frequencies some authors designate this wave as a Stoneley wave [14]). Using [15, eq. (4)], the a_{o-} wave speed as a function of frequency is plotted as a solid line in Fig. 14. As the a_{o-} wave speed asymptotes to the water sound speed of 1440 m/s (dashed line in Fig. 14), radiation into the water increases rapidly [10]. From Fig. 14 (and

referencing [10, Fig. 2]), a better estimate of where this occurs is in the range of 250–350 Hz. In spite of this added complexity, the approximation in (11) is still useful as a simple guide in understanding the associated radiation efficiency variation with frequency [10].

Armed with this background, Figs. 15 and 16 will be discussed and a conjectural physical picture put forth. This discussion will go from top to bottom in Fig. 15 and left to right in Fig. 16. Fig. 15(a) shows the low-frequency precursor seen in Fig. 13(c) starting at about 13.9 s. Fig. 15(b) shows both the

spectrum of this precursor time window (blue) and the background spectrum from several seconds before the event (red). This same background is shown on all panels on the right and allows a visual comparison of the spectral signature of the event, within the time window chosen in each left hand panel, relative to background. Those panels indicate the transition from a signal with main contributions in the tens of hertz to one with contributions from 10 Hz–10 kHz and finally to one whose main contribution is in the hundreds of hertz. Fig. 15(h) also shows magenta and green curves (note that the green curve overlaps on the magenta line for most of the frequency range) that indicate the relative radiation efficiency of the supersonic flexural wave, given the radiation efficiency is proportional to $1/\sqrt{k^2 - k_f{}^2}$, scaled to fit on the spectral curves of the event being studied. (Those curves use (11) to define the critical frequency; from the previous discussion relative to Fig. 14, these curves might shift to the right by 50–100 Hz in more exact modeling of the radiation efficiency.) The green curve assumes an ice thickness of 2 m and the magenta one an ice thickness of 2.5 m. Note that above about 700 Hz, the radiation efficiency curves predict a different falloff with frequency than seen in the data. Two possible explanations are either that the source has little frequency content at higher frequencies or that the simple picture of a constant thickness plate begins to fail as the acoustic wavelength gets small enough to sample the detailed structure of the ice sheet.

The left side of Fig. 16 shows the x, y locations of the ALAS array in magenta and the tracking result for the low-frequency precursor in Fig. 15(a). The precursor tracks to a point above ALAS (note that there is also a sidelobe of the tracking solution near the vertical axis of the left panel in Fig. 16 at around 250 m). One explanation for tracking to a point above ALAS is that the evanescent field for a subsonic flexural wave is passing over the array (this happens before the ice-cracking event itself). When this subsonic wave hits a weak region of the ice, it initiates a cracking event or events. The middle and right panels in Fig. 16 are the tracking results for the first and second pulses seen in Fig. 15(c) that are associated with the actual cracking event(s). The spectrum associated with this time window [see Fig. 15(d)] spans the entire frequency band. The lower frequency components are traceable to a continuation of the low-frequency precursor. The pulses themselves account for the spectrum above about 100 Hz. Previous research [4]–[6] indicates that these types of pulses are evidence of ice cracking. A question motivated by that earlier work is whether the two pulses represent direct acoustic signals from two different cracking events or the first pulse is associated with the supersonic symmetric Lamb wave arrival preceding the direct acoustic signal from a single event [5]. To examine this issue, OASES [16] was used to generate the signals received at ALAS for an explosive source within the ice at $x = 400$ m and $y = 400$ m. The OASES-generated signals show both the symmetric Lamb wave and direct acoustic wave contributions.

Each OASES signal was passed through the tracking processing and the result is shown in Fig. 17. The Lamb wave tracking result is on the left and the direct acoustic wave on the right.
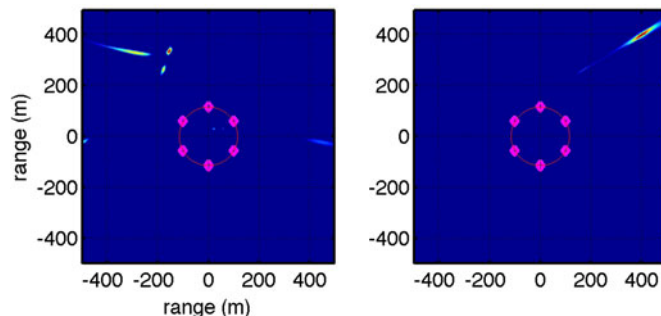

Fig. 17. Tracking results for OASES simulated signals. Left is the tracking result for the symmetric Lamb wave and right is the tracking result for the direct acoustic wave. See text for details.

These two panels are to be compared to the two right panels in Fig. 16. The salient point is that the symmetric Lamb wave path traveling within the ice while coupling energy into the water does not match the assumptions of the tracking model (the largest assumption being straight ray paths between source and receiver) and gives the Lamb wave location at a different angle and range than known to be true. (Obviously one could make a tracking algorithm that would correctly track this wave.) The conclusion derived here from this is that the two pulses seen in Fig. 15(c) are individual acoustic source events within one large cracking event associated with the initial lead formation.

It is important to note that during the day there were 50–60 smaller cracking events along the line where the lead eventually formed. Again, the picture put forth is that the ice was weak along that line and primed for lead formation. A low frequency flexural wave first passed over ALAS and its evanescent field detected, it then propagated past this weakened line and failure occurred (the ice cracked). Furthermore, once the crack was formed it was a point of origin for low frequency subsonic flexural wave energy to scatter into the water that was also detected by the hydrophone. This explanation is in general agreement with proposals from earlier researchers [2], [7]. However, those previous efforts did not have a local lead formation event to dissect in detail.

Left to discuss are the bottom four panels in Fig. 15. Fig. 15(e) and (f) indicates in both the time and frequency domain that low frequency flexural wave energy continues to be present. Around 40 Hz, the signal is lost in the background noise but reappears around 80 Hz and continues to be above the noise until at least 3 kHz. Finally in Fig. 15(g) and (h), the signal rises above the noise at around 100 Hz and begins to converge with the noise floor around 700 Hz. The radiation efficiency curves [see Fig. 15(h)] are used as a basis to conjecture here that the ice, shocked by a lead initiation event, emits a broad spectrum of flexural waves for many seconds and flexural waves with frequencies near the critical frequency are radiated into the water with high efficiency. It is interesting in this regard that the noise floor during this period (the red curves in Fig. 15) shows a drop at around 100 Hz. Given that no local cracking occurred in that background time window, a reason for this could be that the ambient noise energy in this part of the spectrum couples easily into the ice and is absorbed, i.e., the complement to the radiation
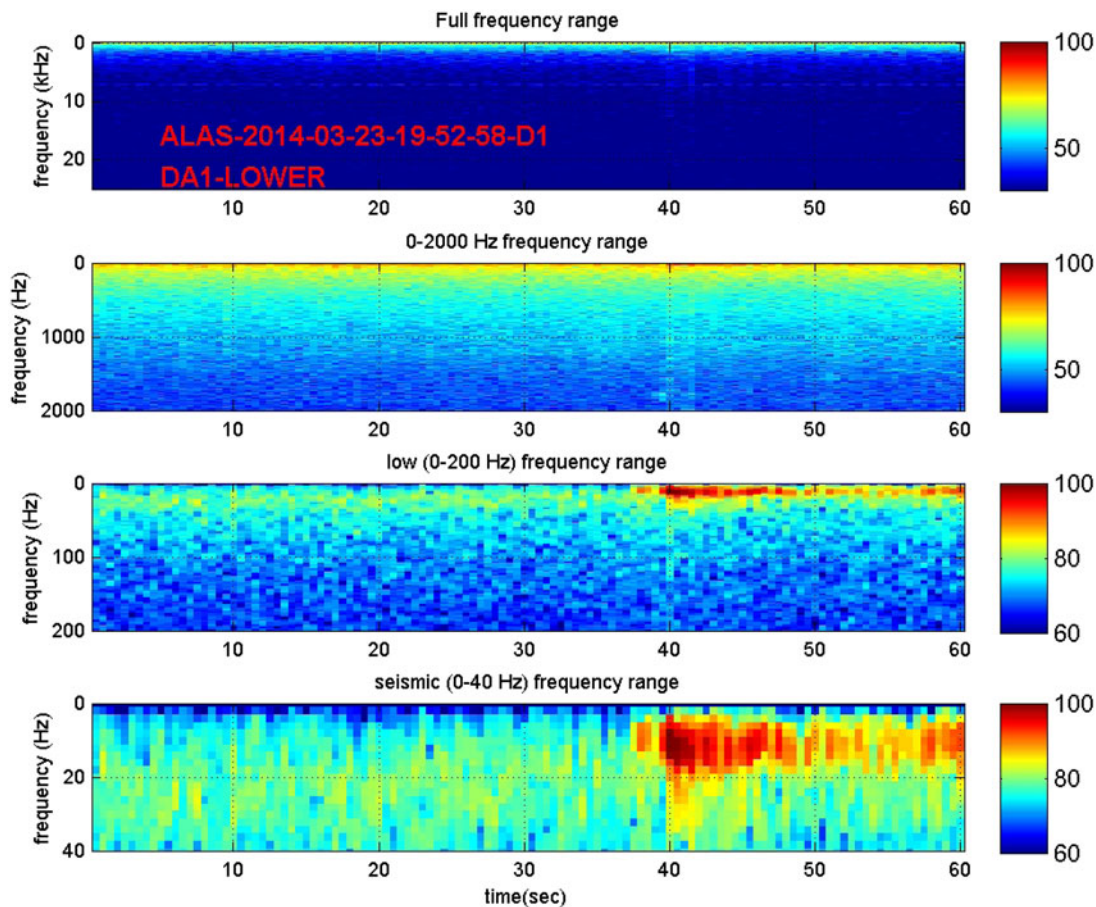
Fig. 18. Time/frequency signature of the seismic event on March 23. Note that the four panels span different frequency ranges so that the details in different frequency bands can be examined. Color bars are in dB re 1 μPa^2/Hz.

into the water from local flexural wave sources. The reader is invited to look back at Fig. 5 and decide if those event signatures further support this picture, i.e., the importance of plate physics in determining the spectrum of the signals received in the water. In particular, the similar structure in the spectrum with helicopter noise (see Fig. 5, red curve) and with ice cracking (see Fig. 5, blue curve) may be due to the energy coupling properties into/out of the plate.

E. Noise Events—Seismic Activity

The Incorporated Research Institutions for Seismology (IRIS) maintains a database of seismic events around the world. IRIS cataloged a seismic event on March 23, 2014 at 19:50:52 at latitude 71.0669 N, longitude 135.363 W, and a depth of 20 km. This location was approximately 415 km from ALAS at a bearing of 96.6° relative to true north. This location is along the Beaufort Sea continental slope. The ALAS array had been restarted only minutes earlier, having been off for several hours due to a low battery condition.

At minute 19:52:58 of March 23, ALAS detected a low-frequency T-wave signal, as shown in Fig 18. The measured time of arrival was 19:53:40 (42 s into the 19:52:58 file). The mechanism of coupling of seismic energy to T-wave energy in the water column has been the subject of research for several

decades. (A recent publication offers an entry into the subject [17].) In the Arctic, experiments have examined T-waves generated by seismic events along the mid-Arctic ridge [3].

Modeling has shown that coupling to T-waves can occur near the event, e.g., along continental slopes and anywhere between the seismic event and the receiver where there is significant interface roughness [17]. For the current case, if the T-wave energy was coupled immediately above the seismic event (assuming a longitudinal speed in the earth of 3500 m/s, an average speed in the water of 1440 m/s, and a water depth of 3500 m) one would predict an arrival around 19:55:45. If, on the other hand, the T-phase energy was coupled at the point where a straight line connects the event and the receiver, the predicted arrival time would be around 19:53:20. The implication is that the T-wave energy was generated somewhere between these two points.

Accounting for the orientation of the ALAS array, the arrival angle of the earthquake is predicted to be 20° relative to the *x*-axis. The tracking results give approximately 13–14°. Given that the estimated error in establishing ALAS rotation relative to North is of order 5°, the difference between estimated and tracked angles is not surprising. (The distance from ALAS (415 km) makes the hyperbolic tracking results for range highly uncertain.) The time-domain signal received for this seismic event at one of the ALAS receivers (30-m depth) and the associated spectral density are shown in Fig. 19.
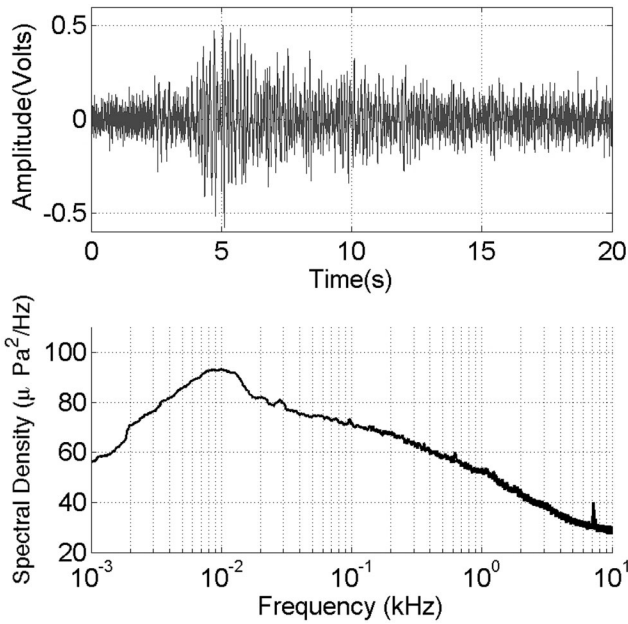
Fig. 19.   Top—The time-domain signal received at one receiver for the seismic event detected on March 23. Bottom—The associated spectral density.

The top panel of Fig. 20 shows 20 s of the seismic data, low pass filtered at 20 Hz. The bottom three panels show modeling results over the same frequency band using a normal mode propagation model (see Appendix) and the source function in the second panel. Those three panels show the received signal for T-wave generation at the bottom/water interface at varying ranges: 103.75, 207.5, and 415 km, respectively, from top to bottom. In each of those panels is the approximate arrival time associated with seismic propagation to the point of coupling followed by T-wave propagation. Since the true source function is not known, the main observation from these model results is the change in the length of the signals due to mode dispersion as a function of distance of propagation in the water.

Comparing the model results to the data, the hypothesis that the coupling occurred somewhere between the seismic source and receivers (derived from the timing) is at least plausible. From a timing standpoint, T-wave coupling about 120–140 km from the receiver would fit the observed arrival time.

Fig. 21 shows the bathymetry derived from [18]. The top panel shows the overall bathymetry with the magenta line going from camp (top/right) to earthquake location (bottom/left). The bottom panel is the depth associated with the magenta line (camp horizontal location is at range = 0 in the bottom panel). The figure indicates the possibility of T-wave generation due to both downslope propagation and interface roughness [17], however, given the slope is actually less than $0.5°$, the downslope coupling may be minimal. The topography near the bottom/right in the top panel of Fig. 21 might also cause out of plane scattering to the receiver.

V. SUMMARY

The experimental results are an important contribution to understanding the current noise environment of the Arctic over
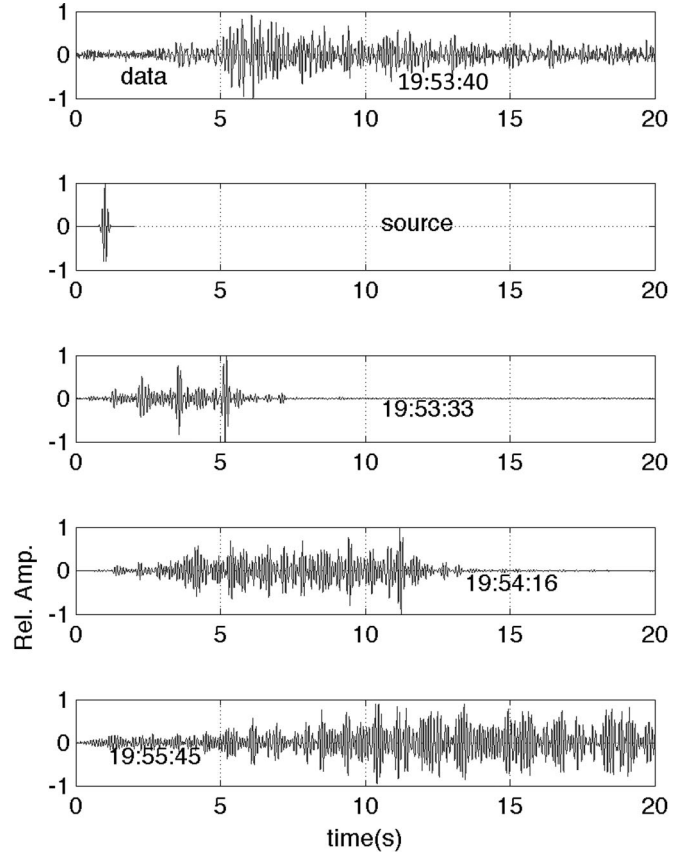

Fig. 20.   Top panel shows 20 s of the seismic data, low pass filtered at 20 Hz. The bottom three panels show modeling results over the same frequency band using a normal mode propagation model and the source function in the second panel. Those three panels show the received signal for T-wave generation at the bottom/water interface at varying ranges: 103.75, 207.5 and 415 km, respectively, from top to bottom. The data and model results have been shifted such that time zero is immediately before wave packet arrival. The times given in the bottom panels are the approximate time of arrival from earthquake to receiver for the seismic event on March 16, given coupling at the associated ranges.
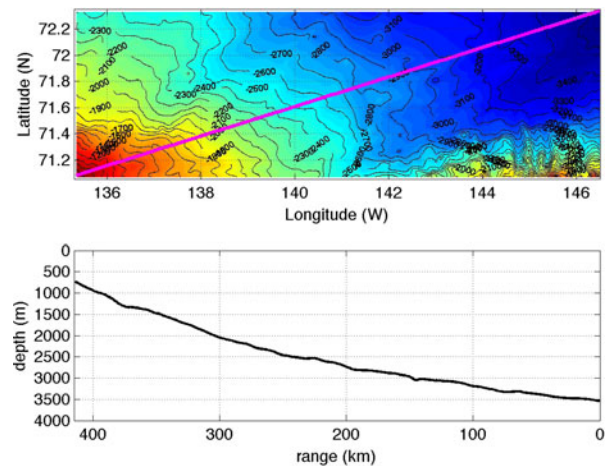

Fig. 21.   Bathymetry derived from [18]. The top panel shows the overall bathymetry with the magenta line going from camp (top/right) to earthquake location (bottom/left). The bottom panel is the depth associated with the magenta line (camp horizontal location is at at range = 0 in the bottom panel).

a large span of frequencies. Knowledge of the time-dependent noise environment is essential when establishing performance limits on sonar systems. Establishing the levels, variations in those levels, and some of the physical mechanisms at play in the modern Arctic were the primary objectives of this paper. Because of this, some effort was spent at presenting the equipment and methods used.

The ALAS array allowed the study of both background noise levels and episodic events over more than four decades of frequency (1 Hz–25 kHz) on a continual basis over the course of two weeks. Both the bandwidth and the continuous monitoring are capabilities that exceed those available in the 80s and 90s when much of the earlier work was carried out. The bandwidth available was important in examining the signals associated with the initial formation of a lead in the near vicinity of the array. Modeling was used as a means of supporting the general picture of the physics involved in generation of the lead-formation acoustics; however, that picture is still highly conjectural. It is hoped that the data will motivate further modeling and perhaps scaled laboratory experiments where environmental parameters can be better controlled and measured.

The detection and timing of the seismic event was aided by the fact that the system was designed to operate nearly continuously (with occasional down times due to logistic constraints). Given those constraints, there was a fortunate congruence of events in the fact that ALAS was operational during the time of the earthquake event. As in the case of the lead opening, modeling was used simply to constrain the possible physics but is not sufficient for definitive conclusions. Having said this, the mode dispersion is a key observable and further modeling using better bathymetric data, when they inevitably become available, will need to capture that dispersion.

APPENDIX

Mode propagation modeling is useful in examining low frequency waveguide propagation (e.g., the T-phase signal associated with an earthquake). Our approach is to develop a framework that includes elastic properties of the seafloor. An acoustic field can significantly penetrate into the seafloor where elastic properties have important effects on propagation at these frequencies. A fully elastic mode code [19], [20] provides the mode functions and horizontal wavenumbers. Using these, a mode-based propagation model for arbitrary pulse waveforms can be developed. Below this mode-based model is formulated in the frequency domain; pulse propagation is determined using Fourier synthesis. The inherent dispersion in mode propagation results in pulse spreading during propagation and can give a qualitative indication of propagation distance within the water column (as done in the main body of the paper).

For a range independent environment, a propagation model based on normal modes is straightforward to formulate. The z-axis is taken to be positive downward with the origin at the sea surface. Assuming the time harmonic case, the pressure $p(R, z)$ is expanded in normal modes as [21]

$$p(R, z) = p_{\text{src}} \sum_n a_n(R)\phi_n(z) \tag{12}$$

where R is the horizontal range coordinate, $a_n(R)$ are mode amplitudes, and $\phi_n(z)$ are mode functions. In general, mode functions and amplitudes are complex, but in this case the mode functions are real because absorption in the seafloor is not included in the elastic mode code. Effects of absorption on mode attenuation are included in mode amplitudes by perturbation theory as described below. In (12), p_{src} is the rms pressure at 1 m. The acoustic source is assumed to be a point source

$$p_o(r) = p_{\text{src}} r_o \frac{\exp(ik_o r)}{r} \tag{13}$$

where $r_o = 1$ m and k_o is the wavenumber at the source depth z_s. For the source given by (13), the mode amplitudes are [21]

$$a_n(R) = \frac{ir_o}{\rho(z_s)} \sqrt{\frac{2\pi}{R}} \exp(-i\pi/4)\phi_n(z_s) \frac{\exp(ik_n R)}{\sqrt{k_n}} \tag{14}$$

where k_n is the horizontal wavenumber for mode n.

When absorption is included in the seafloor, mode horizontal wavenumbers become complex. Assuming the sound speed in the seafloor depends on depth $c_2(z)$, the real wavenumber $k_2(z) = k_{2r}(z) = \omega/c_2(z)$ for a propagating plane wave becomes $k_2(z) = k_{2r}(z) + ik_{2i}(z) \approx k_{2r}(z)(1 + i\delta)$, where the approximate form with the loss parameter δ is often used and gives a linear frequency dependence for absorption.

Ingenito [22] developed the lowest order perturbation result for the imaginary part of the mode horizontal wavenumber accounting for absorption in a sediment half-space with properties independent of depth below a water column of depth D. The result given in [22, A11] is

$$\alpha_n = \frac{k_{2r} k_{2i}}{k_n^{(0)}} \rho_2 \int_D^\infty |\nu_n^{(0)}(z))|^2 dz \tag{15}$$

where α_n is the imaginary part of the horizontal wavenumber for mode n, and therefore it decays according to $\exp(-\alpha_n R)$ when the waveguide boundaries are flat. In (15), the density in the bottom is ρ_2, $k_n^{(0)}$ is the mode horizontal wavenumber for the zero-order problem when attenuation in the bottom is neglected, and $\nu_n^{(0)}(z)$ is the real mode function for the zero-order problem when formulated in terms of the velocity potential. Ingenito assumes that k_{2r}, k_{2i}, ρ_2, and c_2 are constant as a function of depth. If the mode functions are formulated in terms of pressure instead of velocity potential, (15) becomes

$$\alpha_n = \frac{k_{2r} k_{2i}}{k_n^{(0)} \rho_2} \int_D^\infty |\phi_n^{(0)}(z))|^2 dz \tag{16}$$

where $\phi_n^{(0)}(z)$ and $k_n^{(0)}$ are real mode functions and horizontal wavenumbers, respectively. The derivation developed by Ingenito can be generalized to the case where the quantities k_{2r}, k_{2i}, ρ_2, and c_2 all depend on depth. The result is

$$\alpha_n = \frac{1}{k_n^{(0)}} \int_{D_1}^{D_2} \frac{k_{2r}(z)k_{2i}(z)}{\rho_2(z)} |\phi_n^{(0)}(z))|^2 dz \tag{17}$$

where D_1 is the depth of the water, D_2 is the depth at the bottom of the computational region, and the bottom layer has thickness

$D_2 - D_1$. The final complex horizontal wavenumber for mode n is $k_n = k_n^{(0)} + i\alpha_n$. The time-domain pressure is determined by an inverse Fourier transform of (12), having determined the complex horizontal wavenumber at the appropriate frequencies.

REFERENCES

[1] J. H. Ganton and A. R. Milne, "Temperature and wind dependent ambient noise under midwinter pack ice," *J. Acoust. Soc. Amer.*, vol. 38, no. 3, pp. 406–411, 1965.

[2] A. R. Milne, "Thermal tension cracking in sea ice: A source of unknown noise," *J. Geophys. Res.*, vol. 77, no. 12, pp. 2177–2192, 1972.

[3] R. E. Keenan and I. Dyer, "Noise from Arctic Ocean earthquakes," *J. Acoust. Soc. Amer.*, vol. 75, no. 3, pp. 819–825, 1984.

[4] P. J. Stein, "Interpretation of a few ice event transients," *J. Acoust. Soc. Amer.*, vol. 83, no. 2, pp. 617–622, 1988.

[5] A. J. Langley, "Acoustic emission from the Arctic sheet," *J. Acoust. Soc. Amer.*, vol. 85, no. 2, pp. 692–701, 1989.

[6] D. M. Farmer and Y. Xie, "The sound generated by propagating cracks in sea ice," *J. Acoust. Soc. Amer.*, vol. 85, no. 4, pp. 1489–1500, 1989.

[7] N. C. Makris and I. Dyer, "Environmental correlates of Arctic ice-edge noise," *J. Acoust. Soc. Amer.*, vol. 90, no. 6, pp. 3288–3298, 1991.

[8] L. A. Anderson, "Algorithms and error propagation for underwater tracking," Pac. Missile Test Center, Point Mugu, CA, USA, Tech. Rep. 3450-2-78, 1978.

[9] M. V. Greening and P. Zakarauskas, "Pressure ridging spectrum level and a proposed origin of the infrasonic peak in Arctic ambient noise spectra," *J. Acoust. Soc. Amer.*, vol. 95, no. 2, pp. 791–797, 1994.

[10] G. Kaduchak and P. L. Marston, "Observation of the midfrequency enhancement of tone bursts backscattered by a thin spherical shell in water near the coincidence frequency," *J. Acoust. Soc. Amer.*, vol. 93, no. 1, pp. 224–230, 1993.

[11] K. Renji, P. Nair, and S. Narayanan, "Critical and coincidence frequencies of flat panels," *J. Sound Vib.*, vol. 205, no. 1, pp. 19–32, 1997.

[12] P. L. Marston, "GTD for backscattering from elastic spheres and cylinders in water and the coupling of surface elastic waves with the acoustic field," *J. Acoust. Soc. Amer.*, vol. 83, no. 1, pp. 25–37, 1988.

[13] K. L. Williams and R. E. Francois, "Sea ice elastic moduli: Determination of Biot parameters using in-field velocity measurements," *J. Acoust. Soc. Amer.*, vol. 91, no. 5, pp. 2627–2636, 1992.

[14] M. Talmant, G. Quentin, J. Rousselot, J. Subrahmanyam, and H. Überall, "Acoustic resonances of thin cylindrical shells and the resonance scattering theory," *J. Acoust. Soc. Amer.*, vol. 84, no. 2, pp. 681–688, 1988.

[15] P. J. Stein, S. E. Euerle, and J. C. Parinella, "Inversion of pack ice elastic wave data to obtain ice physical properties," *J. Geophys. Res.*, vol. 103, no. C10, pp. 21783–21793, 1998.

[16] H. Schmidt, OASES, Version 2.2 User Guide and Reference Manual, Dept. Ocean Eng., Massachusetts Inst. Technol., Cambridge, MA, USA, 1999. [Online]. Available: http//www.acoustics.mit.edu/henrik/www/oases.html

[17] S. D. Frank, J. M. Collis, and R. I. Odom, "Elastic parabolic equation solutions for T-wave generation and propagation from deep seismic sources," *J. Acoust. Soc. Amer.*, vol. 137, no. 6, pp. 3534–3543, 2015.

[18] M. Jakobsson *et al.*, "The international bathymetric chart of the Arctic ocean (IBCAO) version 3.0," *Geophys. Res. Lett.*, vol. 39, L12609, 2012.

[19] H. Takeuchi and M. Saito, "Seismic surface waves," in *Methods in Computational Physics*, vol. 11, B. A. Bolt, Ed. New York, NY, USA: Academic, 1972, pp. 217–295.

[20] D. J. Doornbus, Ed., *Seismological Algorithms: Computational Methods and Computer Programs*. New York, NY, USA: Academic, 1988.

[21] F. B. Jensen, W. A. Kuperman, M. B. Porter, and H. Schmidt, *Computational Ocean Acoustics*. New York, NY, USA: Springer-Verlag, 2000.

[22] F. Ingenito, "Measurements of mode attenuation coefficients in shallow water," *J. Acoust. Soc. Amer.*, vol. 53, pp. 858–863, 1973.

Kevin L. Williams received the B.S., M.S., and Ph.D. degrees in physics from Washington State University, Pullman, WA, USA, in 1979, 1983, and 1985, respectively.

From 1985 to 1988, he was with the Naval Coastal Systems Center, Panama City, FL, USA, where his primary focus was in acoustic scattering from finite bodies and propagation into ocean sediments. In 1988, he moved to the Applied Physics Laboratory, University of Washington, Seattle, WA, USA, where he worked in the area of high-frequency environmental acoustics (studying propagation through ocean internal waves and Arctic ice and propagation in and scattering from ocean sediments) and understanding the response of targets in the ocean environment.

Dr. Williams is a Fellow of the Acoustical Society of America.
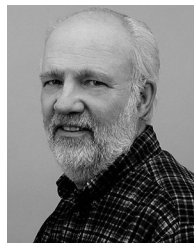
Michael L. Boyd received the B.S. degree in physics and mathematics from Austin College, Sherman, TX, USA, in 1967.

In 1968, he attended graduate school at the University of Texas (UT) before joining UT's Applied Research Laboratory, where he worked on reflection and scattering from the sea surface and from pressure release model surfaces. In 1973, he joined the University of Washington's Applied Physics Laboratory, where his work has generally concentrated on environmental data extraction (inversion), acoustic modeling, sonar performance simulation, underwater guidance and control, and environmental influences on sonar performance. For a number of years, he has also been involved with providing independent validation of several proposed standard performance prediction models (CASTAR, ASPM, GRAB, FeyRay) for the Navy's Oceanographic and Atmospheric Master Library.

Alexander G. Soloway received the B.Eng. degree from McGill University, Montreal, QC, Canada, in 2011, and the M.S. degree from the University of Washington, Seattle, WA, USA, in 2014, both in mechanical engineering. He is currently working toward the Ph.D. degree at the University of Washington, where he is studying the environmental noise from shallow underwater explosions and Scholte wave propagation in sandy sediments.

Eric I. Thorsos received the B.S. degree in physics from Harvey Mudd College, Claremont, CA, USA, in 1965, the M.S. degree in engineering and applied science from the University of California at Davis-Livermore, Livermore, CA, USA, in 1966, and the Ph.D. degree in theoretical nuclear physics from the Massachusetts Institute of Technology, Cambridge, MA, USA, in 1972.

From 1972 to 1975, he was an Assistant Professor of physics with the Hobart and William Smith Colleges, Geneva, NY, USA; from 1975 to 1980, he worked in the area of inertial confinement fusion with the Laboratory for Laser Energetics, University of Rochester, Rochester, NY, USA; and since 1980, he has been in the Applied Physics Laboratory, University of Washington, Seattle, WA, USA. He was the Chief Scientist for SAX99 and SAX04. He is currently a Principal Physicist in the Applied Physics Laboratory and an Affiliate Associate Professor in the Electrical Engineering Department, University of Washington. His research interests include acoustic scattering from the sea surface and the sea bottom, acoustic propagation in shallow water, and electromagnetic scattering at GHz and THz frequencies.

Dr. Thorsos is a Fellow of the Acoustical Society of America and received the Bronze Medal from the National Defense Industrial Association in 1999.

Steven G. Kargl received the B.S. degree in physics and mathematics from the University of Dayton, Dayton, OH, USA, in 1985 and the M.S. and Ph.D. degrees in physics from Washington State University, Pullman, WA, USA, in 1987 and 1990, respectively.

For the next three years, he worked as a Research Physicist with the Coastal Systems Station, Naval Surface Warfare Center, Panama City, FL, USA. In 1993, he joined the Applied Physics Laboratory, University of Washington, Seattle, WA, USA, where he continues to investigate a variety of topics in acoustics. He is currently investigating acoustic penetration into sandy sediments, linear acoustics in a bubbly fluid and nonlinear wave propagation in biological tissue with applications to the formation of thermal lesions. He is currently a Principal Physicist in the Applied Physics Laboratory, University of Washington. His research interests include wave propagation in porous media and ambient noise in littoral waters.

Dr. Kargl is a Fellow of the Acoustical Society of America. From 2000 to 2003, he was an Associate Editor of the *Journal of the Acoustical Society of America* with editorial responsibilities in the areas of ultrasonics and physical acoustics.

Robert I. Odom received the B.S. degree in physics, the M.S. degree in nuclear engineering, and the Ph.D. degree in geophysics from the University of Washington, Seattle, WA, USA, in 1971, 1973, and 1980, respectively.

After two years as an Alexander von Humboldt Fellow in the Seismologisches Zentralobservatorium, Erlangen, Germany, and three years as a Research Staff in the Department of Geological and Geophysical Sciences, Princeton University, Princeton, NJ, USA, he returned to the Pacific Northwest as a Principal Engineer at Boeing; and in 1990, joined the Applied Physics Laboratory, University of Washington. He is currently a Senior Principal Physicist in the Applied Physics Laboratory and a Research Associate Professor in the Department of Earth and Space Sciences, University of Washington. His current research focuses on the bottom interacting underwater acoustics, with a particular emphasis on modeling the effects of bottom elastic properties on shallow water propagation, and the generation of oceanic T-waves.